Molecular Basis for the High CO$_2$ Adsorption Capacity of Chabazite Zeolites

Trong D. Pham,[a] Matthew R. Hudson,[b] Craig M. Brown,*[a, b] and Raul F. Lobo*[a]

CO$_2$ adsorption in Li-, Na-, K-CHA (Si/Al $=$ 6, $=$ 12), and silica chabazite zeolites was investigated by powder diffraction. Two CO$_2$ adsorption sites were found in all chabazites with CO$_2$ locating in the 8-membered ring (8MR) pore opening being the dominant site. Electric quadrupole-electric field gradient and dispersion interactions drive CO$_2$ adsorption at the middle of the 8 MRs, while CO$_2$ polarization due to interaction with cation sites controls the secondary CO$_2$ site. In Si-CHA, adsorption is dominated by dispersion interactions with CO$_2$ observed on the pore walls and in 8 MRs. CO$_2$ adsorption complexes on dual cation sites were observed on K-CHA, important for K-CHA-6 samples due to a higher probability of two K$^+$ cations bridging CO$_2$. Trends in isosteric heats of CO$_2$ adsorption based on cation type and concentration can be correlated with adsorption sites and CO$_2$ quantity. A decrease in the hardness of metal cations results in a decrease in the direct interaction of these cations with CO$_2$.

Introduction

The large-scale capture and sequestration of CO$_2$ from pre-combustion (CO$_2$/H$_2$), post-combustion (CO$_2$/N$_2$), and natural gas mixtures (CO$_2$/CH$_4$) have become important technological and environmental targets to mitigate the effect of greenhouse gases on global climate change.[1] Conventional CO$_2$ capture using primary alkanolamine scrubbers consumes large amounts of energy for regeneration due to the high heat of formation of carbamates and the large heat capacity of the aqueous solution.[2] In addition, this technology uses inhibitors to improve corrosion resistance and prevent oxidative degradation caused by residual oxygen in the flue stream.[3] Nanoporous materials such as carbon molecular sieves,[1b, 4] zeolites,[5] and metal–organic frameworks (MOFs)[6] have been studied for CO$_2$ separations and capture because of their high internal surface area, high micropore volume, chemical tunability, fast adsorption/desorption kinetics, and low heats of adsorption. For zeolitic adsorbents, isosteric heats of adsorption, Q_{st}, on the order of 20 kJ mol^{-1} to 60 kJ mol^{-1} have been measured by techniques such as microcalorimetry[7] and volumetric adsorption measurements.[5b, 8] Spectroscopic techniques have identified a range of adsorbed CO$_2$ surface species in zeolite materials including primarily physisorbed CO$_2$, bidentate carbonates, monodentate carbonates, and carboxylates.[9] By combining variable temperature infrared spectroscopy with periodic DFT calculations, Nachtigall et al. reported that the CO$_2$ adsorption sites could be classified as single- or dual-cation sites in a number of various zeolite types.[10] Molecular simulation methods, such as grand canonical Monte Carlo (GCMC) and molecular dynamics (MD),[11] have been used to study the adsorption of CO$_2$ in porous materials to compute the thermodynamics and transport properties, and identify optimal capture materials. More recently, X-ray and neutron diffraction have been applied to investigate the CO$_2$ adsorption sites in highly crystalline porous materials at the molecular level.[5a, 12]

Chabazite (CHA) is a small-pore zeolite consisting of a double 6-membered ring (D6R) as the basic building unit with one large ellipsoidal cavity accessed by six 8-membered ring windows (8MR) (free aperture $\approx$ 3.8 Å).[13] It is also a model material because it contains only one T-atom (tetrahedral atom: Al or Si atom) in its asymmetric unit. Chabazite-type zeolites provide improved hydrothermal stability over other zeolites, an important property, for example, in the selective catalytic reduction of NO$_x$[14] and moist flue-gas applications. Chabazite has also been shown to have high selectivity for light olefins (ethylene/propylene) in the process of conversion of methanol to olefins and demonstrated potential in gas separation, such as the separation of propane/propene mixtures,[15] and CO$_2$ from N$_2$ in flue gas mixtures[5b, 16] due to its large cavities and small window sizes.

Extra-framework cations present in aluminum-exchanged zeolite frameworks play important roles in determining the adsorption properties of zeolites.[5b, 8b] Cheetham et al.[17] used neutron diffraction and nuclear magnetic resonance while Ugliengo et al.[18] used ab initio periodic calculations to study the location of alkali cations in chabazite zeolites with Si/Al $\approx$ 2.5

[a] T. D. Pham,+ Dr. C. M. Brown, Prof. Dr. R. F. Lobo
Department of Chemical and Biomolecular Engineering
Center for Catalytic Science and Technology
University of Delaware
150 Academy St., Newark, Delaware 19716 (USA)
E-mail: lobo@udel.edu

[b] Dr. M. R. Hudson,+ Dr. C. M. Brown
Center for Neutron Research
National Institute of Standards and Technology
100 Bureau Dr., MS6102 Gaithersburg, Maryland 20899 (USA)
E-mail: craig.brown@nist.gov

[+] These authors contributed equally to this work.

Supporting Information for this article is available on the WWW under http://dx.doi.org/10.1002/cssc.201402555.

These are not the final page numbers! ↗↗

and ≈11, respectively. It was found that K^+ is preferentially located at the 8-membered ring (site SIII'), Li^+ prefers to sit at the 6-membered ring window (6MR, site SII) rather than site SIII (close to the corner of the 4-membered ring, 4MR), and Na^+ is preferentially located at site SII. Additionally, Webley et al.[16b] identified a "trapdoor" filtering mechanism in chabazite zeolites in which CO_2 has sufficient strong interaction to induce large 8MR blocking cations (K^+ and Cs^+) to temporarily deviate from the center of pore apertures for the admission of CO_2 molecules, thus providing a temperature dependent and high selectivity for separation of important industrial gas mixtures such as CO_2/CH_4 and CO_2/N_2.

The impact of zeolite composition on adsorption properties can be observed in comparing the adsorption isotherms of Si-CHA,[8f] Na-CHA-12, and Na-CHA-6[5b] to zeolites NaY (Si/Al = 2.5) and HY40 (Si/Al = 40), showing that siliceous chabazite is, in fact, a better adsorbent than HY40 at room temperature (see the Supporting Information Figure S0). Further, adsorption measurements reveal that the chabazite samples with higher aluminum content have higher adsorption capacity. At 1 atm pressure, the adsorption capacity of Na-CHA-6 is very similar to the adsorption capacity of NaY, and at low pressure, Na-CHA-6 has much higher adsorption capacity.

This report investigates the adsorption properties and site-specific adsorption properties of carbon dioxide in pure, high, and medium silica chabazites (Si-CHA, CHA-12, CHA-6, with Si/Al = ∞, = 12, = 6, respectively). The information is obtained by combining in situ X-ray and neutron powder diffraction methods using Fourier difference mapping to locate the adsorbed CO_2 and correlating this with available volumetric adsorption measurements. The results help elucidate the atomic origin of the adsorption properties across a series of cation-exchanged zeolites which can be the bases for the engineering of improved CO_2 adsorbents.

Result and Discussions

1. Cation locations in chabazite zeolites

To obtain molecular insights into the dominant factors affecting isosteric heat of adsorption and total CO_2 uptake capacity, in situ neutron and X-ray powder diffraction experiments were performed. Rietveld refinements were carried out in the *R-3 m* space group using a hexagonal unit cell containing 36 symmetry-equivalent tetrahedral Si or Al atoms and 72 oxygen atoms for the activated zeolite materials (See the Supporting Information, Tables S3, S8, S11, S14, S16, S19, S22 and Figure S1, S6, S9, S12, S14, S17, S20). Figure 1 depicts the locations of alkali-metal cations typically observed in high-silica chabazites.[18] Lithium and sodium are located at the 6MR window of the hexagonal prism (SII). Fourier difference maps of the activated, dehydrated zeolites indicate that there are no measurable amounts of Li^+ cations in the elliptical cage, at the four-ring (4MR) window of the hexagonal prism, and that no Na^+ cations were found in the 8MR window of the channel (close to site SIII'). The lithium and sodium cations are observed at position SII, as expected, because this coordination environment is
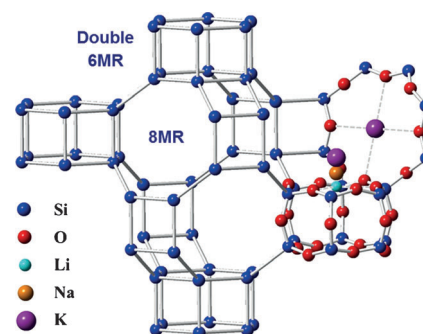

Figure 1. Illustration of the chabazite structure and typical cation locations (Li^+: cyan, Na^+: orange, and K^+: purple) in the zeolite pores (right). 8MR and double 6MR (D6R) are indicated (left, Si/Al: dark blue) with oxygen atoms (red) omitted for clarity.

the most favorable in chabazite for a small cation and is in agreement with the lower alkali-cation concentrations in high-silica chabazites (Si/Al = 6 and = 12).

This is contrast to the low-silica chabazites (Si/Al = 2.5) where cations are additionally located at SIII and close to SIII' as reported by Smith et al.[17] The lithium and sodium locations in the chabazite are very similar to the sites observed in a number of synthetic faujasites, LSX, X, and Y.[19] Each Li^+ or Na^+ is effectively coordinated with 3 oxygen atoms of the chabazite framework. Due to ionic radii difference ($r_{Na+} = 1.16$ Å and $r_{Li+} = 0.73$ Å), Na^+ lies higher above the plane of the 6MR, by an angle of approximately 22° measured from the Si in the ring (Na-CHA-6) compared to Li-CHA-6 with an angle of approximately 9.6°. These angles are slightly larger in the case of Li- and Na-CHA-12, and higher than the values observed for the low-silica zeolites faujasites 13X and Y in which cations are located almost at the center of the ring. In 6MRs with two or three aluminum atoms, cations bind strongly with the basic oxygen atoms [those bonded to Al (O—Al)]. In contrast, in the case of a ring with only one aluminum atom, the cations are situated near the oxygen atoms that are bonded to the Al atom (O—Al) and further from silicon-bonded oxygen (O—Si) atoms giving the longer average distance of the oxygen–cation bond in the 6MR. The out-of-plane location of Li^+ and Na^+ in high-silica chabazites is also due to the contraction of the 6MR due to the smaller average bond lengths of T—O ($d_{Al–O} = 1.76$ Å and $d_{Si–O} = 1.59$ Å).

With respect to Li^+ and Na^+, the bigger K^+ cation sits preferentially in the middle of the 8MR where it is coordinated with four oxygen atoms of the zeolite framework. In addition K^+ is observed on a position above the 6MR (site SII) where it is only coordinated with three oxygen atoms of the zeolite framework. However, this difference is minor since K—O distances in 8MR ($d_{K–O3} = 3.117(4)$ Å, $d_{K–O4} = 3.270(3)$ Å) are longer than the K—O distance in 6MR ($d_{K–O3} = 2.86(6)$ Å).

2. CO_2 adsorption sites in chabazite zeolites

Using GCMC simulation, Bell et al.[11g,h] estimated that dispersive interactions are the primary contributors to the adsorption energy in this sample and are determined by the distances be-

tween the carbon atoms (C_{CO2}) and oxygen atoms (O_{CO2}) of the CO_2 molecule to the surrounding oxygen atoms of the zeolite framework (O_{CHA}). Their calculations suggest equilibrium distances for strong dispersive interaction are $d(O_{CO2}-O_{CHA}) = 3.44$ Å and $d(C_{CO2}-O_{CHA}) = 3.30$ Å, and those contact distances of below 4 Å are considered to have attractive effective van der Waals interactions. The refinement of XRPD and NPD patterns of CO_2 on pure-silica chabazite resulted in the identification of two adsorption sites for CO_2: (1) located in the 8MR and (2) located in the ellipsoid cages of chabazite framework. In the chabazite 8MR, the preferred adsorption site (site A) is the center of the chabazite window in which each carbon atom in CO_2 molecule has maximal close contacts with the eight oxygen atoms of the 8MR (O_{8MR}) such that two O_{8MR} situated across the ring from each other give an angle $O_{8MR}-C_{CO2}-O_{8MR} = 180°$.

From X-ray diffraction refinement of 0.5 CO_2/8MR in Si-CHA, the CO_2–8MR oxygen atom distances were determined to be $d(C_{CO2}-O3) = 3.129(6)$ Å, $d(C_{CO2}-O4) = 3.196(5)$ Å, $d(C_{CO2}-O2) = 3.410(4)$ Å, and with $d(O_{CO2}-O_{CHA})$ between approximately 3.18 and 3.98 Å (Table S26, S27). Another CO_2 adsorption site in pure silica chabazite is situated inside the ellipsoidal cage where the carbon atom has the most effective contact distances with four framework oxygen atoms and the CO_2 oxygen atoms also have effective contact distances with four to five framework oxygen atoms each (site B, Figure 2). The isotropic
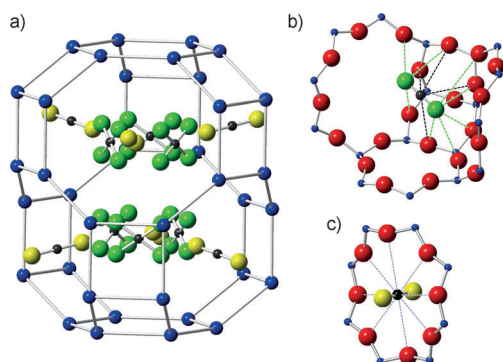

Figure 2. a) CO_2 adsorption sites in pure silica chabazite with framework oxygen atoms omitted for clarity (site A: 8MR, yellow oxygen atoms; site B: cage, green oxygen atoms). b,c) Detailed view of site A CO_2 in the center of the 8 MR (c) and site B with short interaction distances to the red framework oxygens given by dashed lines (b).

atomic displacement parameters (ADPs) for CO_2 in the cage site are higher than those in the window site (Tables S4–S7 and Figure S2–S5), indicating the increase in static disorder of the weaker adsorption sites and possibly a more concave potential energy minimum. Overall, these considerations explain the high occupancy of CO_2 at site A in chabazite zeolites, or indeed in 8 MR zeolites in general.[11g, h]

A physical effect of the adsorption of CO_2 in all-silica chabazite is a slight change in the unit cell parameters, with an initial expansion and, with increased loadings from 0.5 to 1.0 CO_2, evidence of a small contraction on the order of a few thousandths of an Ångstrom (Table S30). There is also a small contraction of the unit cell with increasing measurement tempera-

ture between 10 K neutron and 100 K X-ray diffraction experiments. The negative thermal expansion due to the changes in Si—O—Si interpolyhedral bond angles is also observed in chabazite and other typical siliceous zeolites[20] and typically assigned to the larger amplitude of rigid-unit type modes.[21]

Two CO_2 adsorption sites were determined in Li-CHA and Na-CHA zeolites by Fourier difference map analysis (Figure 3).
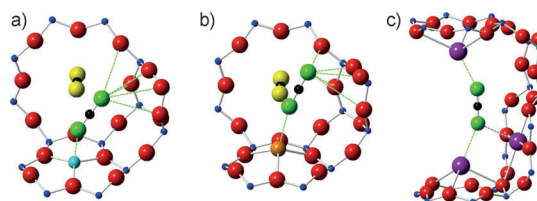

Figure 3. Partial pore views of CO_2 adsorption sites in Li-CHA-6 (a), Na-CHA-6 (b), and K-CHA-6 (c) zeolites. Site A is similar to that previously determined for Cu^{2+}-exchanged chabazite[5a] (indicated by yellow oxygen atoms) and the displacement of the cation (blue Li^+; orange Na^+) strongly influences the coordination of the second CO_2 adsorption site to a site B' with the CO_2 moving closer to the D6R with Li^+. Note that site A, while present in K-CHA-6, has been omitted for clarity in depicting the dual-cation bridged via cation sites SII/SIII' or SII/SII.

The distance between the Na^+ cation and O_{CO2} in site A is much shorter than that for the Li^+ cation (3.605 (0) Å and 4.307 (0) Å in 0.5CO_2/Li-, Na-CHA-6, respectively) leading to a more effective electrostatic interaction (Tables S9, S10, S12, S13, S15, S17, S18 and Figure S7, S8, S10, S11, S13, S15, S16). Further structural details and occupancies of site A in Na-CHA compared to Li-CHA are reported in Table S28. The CO_2 second site in these zeolites is end-on CO_2 coordination with the cation (M^+···O=C=O) where M^+···O=C=O bond distances are longer than the distances of the CO_2 oxygen to the D6R oxygen atoms, $d(Na^+-O_{CO2}) = 2.68$ (7) Å, $d(Li^+-O_{CO2}) = 2.3$ (2) Å and $d(Na^+-O_{CHA}) = 2.447$ (7) Å, $d(Li^+-O_{CHA}) = 2.033$ (5) Å (Table S28). In this configuration, the linear CO_2 molecule is tilted toward the 4MR window to achieve closer contact with other oxygen atoms of the zeolite framework, which is similar to the CO_2 configuration in NaY as reported by Nachtigall et al.[10d] This adsorption site is labeled as site B' since it can be viewed as a rotation and translation of the all-silica site while remaining in the cage.

Since the Li^+···O=C=O distance is shorter than that in Na^+—CHA, the contact angle of the CO_2 is more acute with $\measuredangle Li^+$···O=C=O ≈ 144°, compared to the equivalent $\measuredangle Na^+$···O=C=O ≈ 163°, having more effective dispersive interaction with the zeolite framework and additionally exhibiting close (≈3 Å) interactions with the 6MR oxygen atoms. The resulting high ADPs and coordinate standard deviations for site B' could be the result of slight rotation of the CO_2 around the cation and 4MRs. There is likely a slight position difference across the bulk powder and the model fits the average position. Because the energy contribution of the dispersion interaction and the large quadrupole moment of CO_2 (14.3×10^{-4} °C m²)[22] with an inhomogeneous electric field of zeolite is highest in 8MR zeolites,[5a] site A (at the 8MR) is still a major adsorption site in alkali-ex-

These are not the final page numbers! ↗↗

changed chabazites (Table S26) even though open metal cations provide an additional strong biding site in the cage (site B') through enhanced electrostatic interaction of the adsorbate and adsorbent. The result is also observed in NaA and FER zeolites as reported in the literature.[10d, 12c]

The structure of solid carbon dioxide refined by Peters et al.[23] in space group Pa3, shows that an O atom of the CO_2 molecule is in close contact with more than 10 oxygen atoms of other CO_2 molecules (contact distances of approximately 3.45 Å and 3.18 Å). In Li-CHA, it may be possible to have two molecules in neighbor sites A and B' in the same cage with O—O distances comparable to the ones observed in solid CO_2. Due to the symmetry, however, there could be 3 possible positions of CO_2-site B' around the Li$^+$ cation, and the stable configuration of CO_2 sites A and B' coexisting in the same cage is one in which site B' is in close contact with the 4MR opposite to site A ($d_{O-O} = 3.105$ Å, Figure S23). Moreover, in solid CO_2, the C atom has close contact with 6 oxygen atoms of other CO_2 molecules ($d_{C-O} \approx 3.11$ Å), which is the distance we found in the 8MR due to the interaction between the partially positive charge of C_{CO2} and the negative charge of O in the zeolite framework. This is also observed in Na-CHA. In the cases of low CO_2 doses in Li- and Na-CHA-12, there is an overall similarity of the positions and occupancies of the two CO_2 sites with $\angle$ Li$^+$···O=C=O $\approx 142°$, $\angle$ Na$^+$···O=C=O $\approx 166°$, and the Li$^+$—O$_{CO2}$ and Na$^+$—O$_{CO2}$ (site B') distances are identical to those in Li-/Na-CHA-6 at 2.302(5) Å and 2.59(8) Å, respectively, (Tables S26, S28 and Figure S24, S25).

Refinement of the K-CHA-12 data (Tables S20, S21, and Figure S18, S19) show that K$^+$ behaves quite similarly to Cu^{2+} in that the majority of the CO_2 is found in the 8MR and only a small fraction of the adsorbate is found with an end-on CO_2 coordination with the cations (Tables S26, S29). Interestingly, in K-CHA-6 with the higher concentration of K$^+$ in both SII and SIII' (partially blocking more of the 8MR window), the occupancy of the second CO_2 site (site C) in the cage is significantly increased (Tables S23, S24, and Figure S21, S22). The increase in interaction energy is due to the CO_2 coordination to two K$^+$ cations (either cations in sites SII/SIII' or SII/SII) being more efficient in lower silica K-CHA-6 with a distance from O$_{CO2}$ to K$^+$ of approximately 3 Å. Nachtigall et al. reported this as the dual-cation site.[10] In this configuration, the oxygen and carbon atoms also have a number of attractive interactions with framework oxygen atoms (Figure S26). From Fourier analysis, there is some disorder indicated from adsorption at site C in K-CHA as this site can be coordinated with potassium, either by single- or dual-cation sites, resulting in an average CO_2 position with high ADPs. Various models for the configuration of site C were considered and this location (with high ADPs), shown in Figure 3, resulted in the best refinement.

3. Adsorption Properties of Sodium-Exchanged Zeolites

Chemical analysis of the samples by ICP and EDX (see Table S1) show that Si/Al ratios for the chabazite samples are near the expected Si/Al = 12 for CHA-12, and Si/Al = 5.95–6.6 for CHA-6 samples. The ratio of cation (Li, Na, and K) to Al is close to one in all cases. Si-CHA, Li-CHA, and Na-CHA have a microporous volume determined by the t-plot method of approximately 0.27 cc g^{-1}, while, for both potassium samples, the microporous volume is much lower (0.18–0.20 cc g^{-1}). This is in part due to the larger size of potassium cations, but may reflect the presence of some inaccessible cages.

CO_2 adsorption isotherms, isosteric heats of adsorption, and the adsorption capacity of Na-chabazite zeolites are compared to selected commercial zeolites samples at 1 bar and 303 K in Table 1 (and Figure S0). At low loadings, NaA and Na13X have

Table 1. Adsorption parameters of select chabazite zeolites compared to select commercial zeolites at 1 bar and 303 K.

Adsorbents	Na13X	NaY	NaA	Na-CHA-6	Na-CHA-12	Na-FER[25]	Si-CHA	HY40
Si/Al ratio	1.25	2.47	1	6	12	8.7	∞	40
Micropore vol. [cm^3 g^{-1}]	0.29	0.31	0.21[a]	0.25	0.27	0.12	0.27	0.3
Capacity [mmol g^{-1}]	5.2	5.1	4.1	5.0	4.0	2.6	1.9	0.6
$-Q_{st}$ [kJ mol^{-1}]	51.5	35	53.4	43.0	41.3	45.2	24	17.4

[a] N_2 is not able to access the pores of NaA; micropore volume at a relative pressure of 0.029 P/P_0 calculated from CO_2 adsorption at 0 °C was taken from ref. [26].

higher adsorption capacity than Na-CHA-6, as expected due to the high cation density of low-silica zeolites. On the other hand, Si-CHA has a higher adsorption capacity than HY40 up to 1 bar. GCMC simulations[11c, g, h] and DFT calculations[10] have shown the importance of dispersive interaction between CO_2 and the walls of microporous materials. This explains why the isosteric heats of CO_2 adsorption on chabazite zeolites are higher than those in faujasite zeolites; specifically Na-CHA-6 > NaY, and Si-CHA > HY40 even though faujasites have higher charge density than the chabazite samples. At high loading, the adsorption capacity depends on both the relative strength of adsorbate–adsorbent interactions and the micropore volume of the adsorbents.[5b, 24]

The equilibrium CO_2 capacity of Na-CHA-6 is 5.0 mmol CO_2 per gram of zeolite at 303 K and 1 bar, which is comparable to the value of zeolites Na13X and NaY, but appreciably higher than that of NaA, even though the cation density in Na-CHA-6 is significantly lower. Note that the amount adsorbed and the isosteric heat of adsorption of Na-CHA-6 is higher than those of Na-CHA-12 and Si-CHA as expected for increasing concentration of Al^{3+} in the zeolite framework. Ferrierite containing 8- and 10-ring straight channels showed slightly higher heats of adsorption at zero coverage, but significantly lower adsorption capacity (Table 1) as compared to Na-CHA-12 with similar Si/Al ratio due to its smaller pore size and much smaller micropore volume.

These are not the final page numbers! ↗↗

4. Structure-property relationship: CO₂ adsorbed on chabazite zeolites

In cation-exchanged zeolites, the cations act as Lewis acid sites and the framework oxygen atoms, bearing partial negative charges, behave as basic sites. The basicity of framework oxygen atoms of alkali-exchanged zeolites is in the order of $Li^+ < Na^+ < K^+ < Cu^{2+}$ based on local hard–soft acid–base (HSAB) descriptors.[27] Based on this principle, the interaction between the Lewis acid site (the carbon in CO_2) and basic zeolite oxygen atoms is the highest in Cu^{2+} and is the lowest in Li^+. This observation accounts for the very high occupancy of CO_2 in the middle of 8MR in Cu-CHA-6 and the lowest occupancy in Li-CHA.[5a] Extra-framework cations are hard Lewis acid sites following the order of $Li^+ > Na^+ > K^+ > Cu^{2+}$ while O atoms in CO_2 act as hard base sites. Given that hard–hard and soft–soft interactions dominate the hard–soft interactions as demonstrated in HSAB theory, the end-on CO_2 coordination with these cations ($M^{n+}\cdots O=C=O$) is more stable in Li^+ than in other cation sites. This was also observed in the adsorption of the O-atom (in the CH_3OH molecule) on alkali-exchanged faujasite ($Li^+ > Na^+ > K^+ > Rb^+ > Cs^+$).[28] This explains the highest CO_2 occupancy in the second site for Li^+ and the lowest occupancy in Cu-CHA-6 (Table S26, Ref. [5a]).

Figure 4 shows the isosteric heats of adsorption as a function of CO_2 loading for all CHA samples. There is a noticeable decrease in $-Q_{st}$ with increased CO_2 quantity due to a decrease in the electric field. Based on very similar location of cations Li^+ and Na^+ in the chabazite framework, Li-CHA and Na-CHA have quite similar CO_2 adsorption capacities and heats of adsorption (Figure 4 and Ref. [5b]). As per above, Li^+ is located closer to the 6MRs than Na^+ and leaves more empty space for the adsorbate. Therefore, at 1 atm, the adsorption capacity of CO_2 in Li-CHA-6 is slightly higher than in Na-CHA-6 (5.1 mmol g^{-1} and 5.0 mmol g^{-1}, respectively [5b]). The adsorption site B' in Li-CHA has higher energy than in Na-CHA, but this site only adsorbs a maximum of 5.2 CO_2 uc$^-$, while site A allows for a maximum of 9 CO_2 uc$^-$ (uc = unit cell). This higher dependence of interaction energy on Li^+, or the higher consumption of Li^+ cation by coordinating with adsorbates at high CO_2 coverage, could be the reason for a faster drop of the heats of adsorption on Li-CHA over CO_2 loading amounts as compared to Na-CHA adsorbents. This result is consistent with the study on Li-, Na-, K-ZSM-5 by Nachtigal et al.[10d]

The electric field in K-CHA-12 is lower than that in Li-, Na-CHA-12 due to its larger cationic size. Thus, a lower adsorption heat at zero coverage was observed for K-CHA-12. As discussed earlier, most of CO_2 in K-CHA-12 is located in the 8MR (accommodating a maximum of 9 CO_2 uc$^-$ on this site) is less susceptible to the electric field generated by potassium cations. This explains a slight drop in heat of adsorption on this sample. A dual-cation site is more effective in K-CHA-6 due to higher possibility of two K^+ ions (site SII) located in one cage or one located in the 6MR with a distance of approximately 7.5 Å to the other K^+ in the 8MR. The formation of the dual-site cation leads to comparable adsorption heat for this sample at zero coverage as compared to zeolites Li-, and Na-
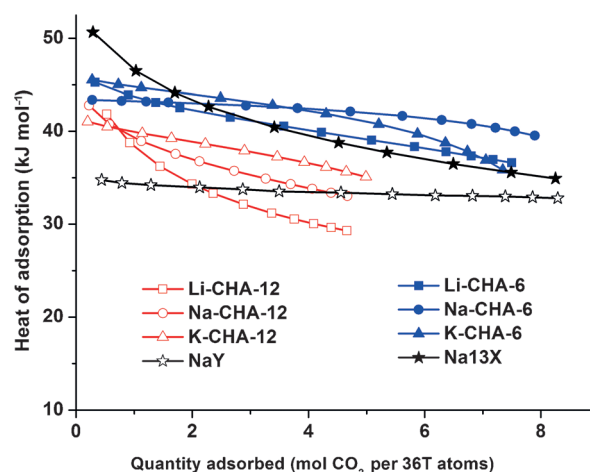

Figure 4. Isosteric heats of CO_2 adsorption ($-Q_{st}$) on chabazite zeolites and faujasite zeolites as a function of amount adsorbed. *36 T atoms are equal to 1 unit cell (uc) of chabazite and 3/16 uc of faujasite zeolites.

CHA-6. At higher loading of CO_2 ($> 6 CO_2$/uc), when the dual-cation and 8MR adsorption sites are mostly occupied, the heats of adsorption drops faster than in Li- and Na-CHA-6. The lower adsorption heat in Cu-CHA-6 (33.1 kJ mol^{-1})[5a] associated with the depopulation Cu^{2+} cation content (compared to alkali-cations) leads to a decrease of electric field in the zeolite. In addition, the lower electrostatic energy between CO_2 and Cu^{2+} is due to the fact that the major adsorption site of CO_2/Cu-CHA-6 is in the 8MR, whereas the largest electric field is located around Cu^{2+} in the D6R.

Low dispersion interaction energy is observed in large cages, and according to Bell[11e] and Nachtigall,[10d] the adsorption sites of CO_2 in low-silica faujasites reflect a high level of interaction with Na^+ cations instead of interaction with the framework, as observed here for small-pore chabazites. In NaY, most Na^+ cations coordinate to 6MRs inside the sodalite cages, where they are inaccessible to the adsorbate; thus, the adsorption energy in NaY is lower than that in high-silica chabazite zeolites. The presence of Na^+ site SIII in low-silica faujasite Na13X has led to the formation of dual-cation adsorption sites.[10d] Thus, Na13X has the highest adsorption heat at low CO_2 coverage among the studied zeolites and a steep drop in the heats of adsorption due to the high consumption of cation sites with high CO_2 loading amount. Because of the high dependence of the CO_2 adsorption on the cations in faujasite zeolites, the presence of water and other polar molecules in flue gas streams will dramatically decrease their CO_2 adsorption capacity, making this class of zeolites less efficient and impractical compared to high-silica chabazites

Conclusions

Structural analysis of cation-exchanged high- and pure-silica chabazites was performed with in situ CO_2 gas loading by X-ray and neutron diffraction and the relationship of zeolite structures to their adsorption energy interactions was discussed. Site A (8MR) was identified as the major CO_2 adsorp-

These are not the final page numbers! ↗↗

tion site in pure-silica chabazites due to the high number of close contacts to the framework oxygen atoms to the CO_2. Li^+ and Na^+ cations were only observed at site SII of the D6R, where the larger K^+ cation can occupy D6R and 8MR. These exchanged cations in chabazites are all open metal ions providing strong binding sites through induced polarizability of the adsorbate, whereas the majority of these cations residing in sodalite cages of zeolites A and faujasites are not accessible to adsorbates. Carbon dioxide is coordinated end-on to alkali-metal cations ($M^+ \cdots O = C = O$) with the molecular axis tilted to the 4MR to maximize its dispersion interaction with the framework oxygens. High disorder of the second adsorption site in K-CHA, particularly K-CHA-6, is due to a mixed population of single- and dual-cation adsorption sites in the chabazite cage. The population of the direct coordinated adsorption sites of CO_2 with these metal cations decreases with the hardness of cation $Li^+ > Na^+ > K^+ > Cu^{2+}$, except for the case of K-CHA-6, where the bridged complexes of CO_2 and two K^+ cation sites were formed with higher interaction energy than a single cation adsorption site. Additionally, a major CO_2 adsorption site in the 8 MR (site A) was still observed in these cation-exchanged chabazites due to high van der Waals and quadrupole interactions. At low CO_2 coverage, the heats of adsorption in Li-, Na-, and K-CHA are quite similar due to the inverse effect of electric fields caused by cations and basicity caused by framework oxygens. A faster drop of heat of adsorption over the CO_2 loading amount in Li-CHA compared to Na-CHA is due to a higher dependence of the interaction energy on Li-exchanged adsorbents.

Experimental Section

Zeolite Materials

Zeolite NaA (Si/Al = 1) was purchased from Sigma Aldrich Na13X (Si/Al = 1.25) and NaY (CBV100, Si/Al = 2.47), HY (CBV780, Si/Al = 40) were purchased from Zeolyst. (Please note: any mention of commercial products is for information only; it does not imply recommendation or endorsement by NIST.)

Pure silica chabazite Si-CHA:[8f, 29] 11.8 g of TEOS was hydrolyzed in 23.9 g of TMAdaOH and heated to remove the ethanol and water (23.8 g in total). Then 1.2 g of HF was added to the mixture to produce the final composition of $3 H_2O : 1 SiO_2 : 0.5\ TMAdaOH : 0.5\ HF$. This thick paste was homogenized by hand in a Teflon container, and transferred to a 23 mL Teflon-lined stainless steel autoclave (Parr). The autoclave was kept at 423 K with rotation (~40 rpm) for 48 h in a convection oven. The as-made product was then calcined in air at 873 K for 16 h heating at a ramping rate of 5 K min^{-1} to prepare Si-CHA.

CHA-6 (Si/Al = 6):[5b, 14b] A solution of 10 g of sodium silicate (Sigma Aldrich, 26.5 % SiO_2), 0.32 g of NaOH (Fisher Scientific, > 98 %) and 24 g of DI water was stirred at room temperature for about 15 min. Then, 1 g of Na-Y (Zeolyst CBV100, Si/Al = 2.47) and 1.6 g of N,N,N-trimethyl-1- adamantanammonium iodide were added to the solution and stirred for another 30 min. The resulting solution was then transferred into 43 mL Teflon-lined autoclaves (Parr) and heated at 423 K under rotation for 6 d. The solid product was separated by vacuum filtration, washed extensively with DI water, and dried at 353 K overnight. The as-made product was then calcined

in air at 823 K for 8 h using a ramping rate of 5 K min^{-1} to prepare the starting form of Na-CHA-6.

CHA-12 (Si/Al = 12):[5b] A mixture of tetraethyl orthosilicate (TEOS, sigma 98 %), N,N,N-trimethyl-1-adamantanamine hydroxide (TMA-daOH, 25 % wt., Sachem Inc.) and DI water were mixed for 2 h, then Al(OEt)$_3$ (Strem Chemical, 99 %) was added to the solution to obtain a final gel composition of $SiO_2 : H_2O : TMAdaOH : Al_2O_3$ is 1 : 20 : 0.5 : 0.035 and stirred for another 12 h. The resulting solution was then transferred into Teflon-lined autoclaves and heated at a temperature of 423 K under static condition for 6 d. After that, the sample was washed with DI water, and dried at 353 K overnight. The as-made product was then calcined in air at 823 K for 8 h heating at a ramping rate of 5 K min^{-1} to prepare the starting form of H-CHA-12.

Ion Exchange

Ammonium exchanged NH$_4$-CHA (Si/Al = 6, = 12) was prepared by mixing 1 g Na-CHA-6 (or H-CHA-12) with 500 mL NH$_4$NO$_3$ 0.1 M overnight at 353 K. The solution was then filtered and washed with deionized water, and the resulting NH$_4$-CHA product was dried at 353 K overnight. The ion-exchanged Li-CHA, Na-CHA, K-CHA were prepared by mixing 0.1 g NH$_4$-CHA and 50 g 2 M LiCl ($\geq$ 99.0 %, Sigma), NaCl ($\geq$ 99.0 %, Sigma), KCl ($\geq$ 99.0 %, Sigma) for 12 h at 353 K respectively, and the resulting cation-exchanged CHA products were dried at 353 K overnight. The ion exchange was repeated several times to obtain the completely exchanged form of alkali-metal chabazites. Compositions of metals in cation-exchanged chabazites were determined by inductively coupled plasma mass spectrometry (ICP) and energy-dispersive X-ray spectroscopy (EDX) methods (Table S1). Porosity and surface areas of all zeolite materials were characterized by 77 K N$_2$ adsorption (Table S2).

Powder Diffraction

Neutron powder diffraction (NPD) experiments were carried out on activated chabazite zeolites using the high-resolution neutron powder diffractometer, BT1, at the National Institute of Standards and Technology Center for Neutron Research (NCNR). All samples (neutron and X-ray) were activated (dehydrated) by turbomolecular pump while heating at a temperature of ca. 250 °C for 18–24 hrs. The evacuated samples were placed in a He purged glove box, each loaded into a vanadium can equipped with a gas loading valve, and sealed using an indium O-ring. NPD data were collected using a Ge(311) monochromator with an in-pile 60′ collimator corresponding to a wavelength of 2.0782 Å. The samples were loaded onto a bottom-loading closed cycle refrigerator, glove box He evacuated by turbomolecular pump (RT) and data were collected on the bare frameworks at 10 K. For the *in situ* NPD runs, the samples were warmed to 300 K and then exposed to a predetermined amount of CO$_2$ gas from a volumetric gas manifold. Upon reaching an equilibrium pressure at the loading temperature, the sample was then slowly cooled to ensure equilibrium and complete adsorption of the CO$_2$ (< 1 K min^{-1}). Data were again collected at 10 K reducing the thermal motions for the framework and adsorbate.

Similarly, synchrotron X-ray powder diffraction (XRPD) data for pure silica chabazite and K-CHA-6 were measured at the Advanced Photon Source (APS) at Argonne National Laboratory on the 1-BM materials diffractometer (λ = 0.6124 Å). For XRPD measurement, adsorbents were activated, as described previously, loaded into glass capillaries, and attached to a valve assembly via ultra-Torr fitting all while inside a N$_2$ glove box. N$_2$ was evacuated from the samples

in-line via turbomolecular pump and then samples were dosed with known quantities of CO_2 using a custom built gas dosing manifold of known volume. Data were collected at 100 K to again reduce thermal parameters in the materials. Reasons for collecting synchrotron XRPD data on the two selected samples (Si-CHA and K-CHA-6) are as follows: In the case of Si-CHA, the very low affinity for CO_2 adsorption led to questions about the positional accuracy of the refinements from initial NPD and so higher resolution XPRD was considered to remove questions of ambiguity. For K-CHA-6, based on the fact that large cation mobility has been observed in other CHA samples when CO_2 adsorption is considered,[16b, c, 30] XPRD measurements were warranted due the relatively low coherent neutron scattering cross section for potassium (around half that of Si, C, O) vs. higher X-ray scattering cross section (relative to C, O) for K. Accurately determining the positions of the K^+ cations compared with that of CO_2 are critical.

Rietveld refinements were carried out using the EXPGUI package/ GSAS for NPD and XPRD data.[31] Further details of the crystal structure investigations may be obtained from the Fachinformationszentrum Karlsruhe, 76344 Eggenstein-Leopoldshafen, Germany (fax: (+49) 7247-808-666; e-mail: crysdata@fiz-karlsruhe.de) on quoting the deposition numbers CSD (-427822, -427823, -427824, -427825, -427826, -427827, -427828, -427829, -427830, -427831, -427832, -427833, -427834, -427835, -427836, -427837, -427838, -427839, -427840, -427841, and -427842). For the zeolite frameworks, the occupancy of aluminum (vs. Si) is too small to be accurately determined with NPD and to reduce the variables in the Rietveld refinement was fixed based on the average compositions measured by ICP and EDX methods (Table S1). Similarly, since ICP and EDX can better determine sample composition than powder diffraction, the extra-framework cations occupancies are fixed at values from the ICP and EDX since no observable impact on the quality of the refinement is noted.

Fourier difference methods were then employed to elucidate the adsorbed molecules in the data collected from the samples subsequently loaded CO_2. This has been described previously.[5a] CO_2 doses that range from 0.33 to 0.66 CO_2 molecules per 8MR window in the CHA-12 samples and 0.5 to 1.0 CO_2 molecules per 8MR window in CHA-6 were chosen based on simplifying the discussion (and refinements) in these materials. Keeping the occupancy of CO_2 lower in the low-cation exchanged materials is key to determining the primary adsorption site. Similarly, not exceeding one CO_2 molecule per 8MR in the CHA-6 samples allows for either full adsorption at the window site or occupation of a secondary site while reducing the likelihood of potential bulk like disorder. Additional refinement details include the restraining of the CO_2 angle in the secondary sites (sites B, B′, C as subsequently discussed) to be 180°, and the restraint of CO_2 bond distance to $d_{C-O}(CO_2) = 1.16$ Å (due to the symmetric nature of the CO_2 across symmetry sites, bonds tended to an "average" longer than ideal), and atomic displacement parameters (ADPs) and fractional occupations for C and O in the same site CO_2 were constrained to be the same as well for clarity.

Acknowledgements

[1] a) Y. S. Bae, R. Q. Snurr, *Angew. Chem. Int. Ed.* **2011**, *50*, 11586–11596; *Angew. Chem.* **2011**, *123*, 11790–11801; b) N. Hedin, L. J. Chen, A. Laaksonen, *Nanoscale* **2010**, *2*, 1819–1841.

[2] A. B. Rao, E. S. Rubin, *Environ. Sci. Technol.* **2002**, *36*, 4467–4475.

[3] a) D. M. D'Alessandro, B. Smit, J. R. Long, *Angew. Chem. Int. Ed.* **2010**, *49*, 6058–6082; *Angew. Chem.* **2010**, *122*, 6194–6219; b) G. T. Rochelle, *Science* **2009**, *325*, 1652–1654.

[4] S. Choi, J. H. Drese, C. W. Jones, *ChemSusChem* **2009**, *2*, 796–854.

[5] a) M. R. Hudson, W. L. Queen, J. A. Mason, D. W. Fickel, R. F. Lobo, C. M. Brown, *J. Am. Chem. Soc.* **2012**, *134*, 1970–1973; b) T. D. Pham, Q. L. Liu, R. F. Lobo, *Langmuir* **2013**, *29*, 832–839; c) J. Kim, L. C. Lin, J. A. Swisher, M. Haranczyk, B. Smit, *J. Am. Chem. Soc.* **2012**, *134*, 18940–18943; d) O. Cheung, N. Hedin, *RSC Adv.* **2014**, *4*, 14480–14494.

[6] a) K. Sumida, D. L. Rogow, J. A. Mason, T. M. McDonald, E. D. Bloch, Z. R. Herm, T. H. Bae and J. R. Long, *Chem Rev* **2012**, *112*, 724–781; b) L. C. Lin, J. Kim, X. Q. Kong, E. Scott, T. M. McDonald, J. R. Long, J. A. Reimer, B. Smit, *Angew. Chem. Int. Ed.* **2013**, *52*, 4410–4413; *Angew. Chem.* **2013**, *125*, 4506–4509; c) Y. Y. Liu, Z. Y. U. Wang, H. C. Zhou, *Greenhouse Gases Sci. Technol.* **2012**, *2*, 239–259; d) P. Nugent, Y. Belmabkhout, S. D. Burd, A. J. Cairns, R. Luebke, K. Forrest, T. Pham, S. Q. Ma, B. Space, L. Wojtas, M. Eddaoudi, M. J. Zaworotko, *Nature* **2013**, *495*, 80–84.

[7] a) J. A. Dunne, R. Mariwals, M. Rao, S. Sircar, R. J. Gorte, A. L. Myers, *Langmuir* **1996**, *12*, 5888–5895; b) J. A. Dunne, M. Rao, S. Sircar, R. J. Gorte, A. L. Myers, *Langmuir* **1996**, *12*, 5896–5904.

[8] a) Q. L. Liu, T. Pham, M. D. Porosoff, R. F. Lobo, *ChemSusChem* **2012**, *5*, 2237–2242; b) G. D. Pirngruber, P. Raybaud, Y. Belmabkhout, J. Cejka, A. Zukal, *Phys. Chem. Chem. Phys.* **2010**, *12*, 13534–13546; c) R. Bulánek, K. Frolich, E. Frydova, P. Cicmanec, *Top. Catal.* **2010**, *53*, 1349–1360; d) J. Zhang, R. Singh, P. A. Webley, *Microporous Mesoporous Mater.* **2008**, *111*, 478–487; e) P. J. E. Harlick, F. H. Tezel, *Microporous Mesoporous Mater.* **2004**, *76*, 71–79; f) T. D. Pham, R. Xiong, S. I. Sandler, R. F. Lobo, *Microporous Mesoporous Mater.* **2014**, *185*, 157–166.

[9] a) R. W. Stevens, R. V. Siriwardane, J. Logan, *Energy Fuels* **2008**, *22*, 3070–3079; b) P. A. Jacobs, F. H. van Cauwelaert, E. F. Vansant, *J. Chem. Soc. Faraday Trans. 1* **1973**, *69*, 2130–2139; c) T. Montanari, G. Busca, *Vib. Spectrosc.* **2008**, *46*, 45–51.

[10] a) C. Otero Areán, M. R. Delgado, G. F. Bibiloni, O. Bludsky, P. Nachtigall, *ChemPhysChem* **2011**, *12*, 1435–1443; b) P. Nachtigall, M. R. Delgado, D. Nachtigallova, C. O. Arean, *Phys. Chem. Chem. Phys.* **2012**, *14*, 1552–1569; c) A. Pulido, P. Nachtigall, A. Zukal, I. Dominguez, J. Cejka, *J. Phys. Chem. C* **2009**, *113*, 2928–2935; d) L. Grajciar, J. Cejka, A. Zukal, C. O. Arean, G. T. Palomino, P. Nachtigall, *ChemSusChem* **2012**, *5*, 2011–2022.

[11] a) L. C. Lin, A. H. Berger, R. L. Martin, J. Kim, J. A. Swisher, K. Jariwala, C. H. Rycroft, A. S. Bhown, M. Deem, M. Haranczyk, B. Smit, *Nat. Mater.* **2012**, *11*, 633–641; b) A. Garcia-Sanchez, C. O. Ania, J. B. Parra, D. Dubbeldam, T. J. H. Vlugt, R. Krishna, S. Calero, *J. Phys. Chem. C* **2009**, *113*, 8814–8820; c) R. Krishna, J. M. van Baten, *Sep. Purif. Technol.* **2008**, *61*, 414–423; d) R. Krishna, J. M. van Baten, *Microporous Mesoporous Mater.* **2011**, *137*, 83–91; e) G. Maurin, P. L. Llewellyn, R. G. Bell, *J. Phys. Chem. B* **2005**, *109*, 16084–16091; f) M. Fischer, R. G. Bell, *J. Phys. Chem. C* **2013**, *117*, 24446–24454; g) M. Fischer, R. G. Bell, *J. Phys. Chem. C* **2013**, *117*, 17099–17110; h) M. Fischer, R. G. Bell, *J. Phys. Chem. C* **2012**, *116*, 26449–26463; i) H. J. Fang, P. Kamakoti, J. Zang, S. Cundy, C. Paur, P. I. Ravikovitch, D. S. Sholl, *J. Phys. Chem. C* **2012**, *116*, 10692–10701.

These are not the final page numbers! ↗↗

[12] a) M. M. Lozinska, E. Mangano, J. P. S. Mowat, A. M. Shepherd, R. F. Howe, S. P. Thompson, J. E. Parker, S. Brandani, P. A. Wright, *J. Am. Chem. Soc.* **2012**, *134*, 17628–17642; b) W. L. Queen, C. M. Brown, D. K. Britt, P. Zajdel, M. R. Hudson, O. M. Yaghi, *J. Phys. Chem. C* **2011**, *115*, 24915–24919; c) T. H. Bae, M. R. Hudson, J. A. Mason, W. L. Queen, J. J. Dutton, K. Sumida, K. J. Micklash, S. S. Kaye, C. M. Brown, J. R. Long, *Energy Environ. Sci.* **2013**, *6*, 128–138; d) H. Wu, J. M. Simmons, G. Srinivas, W. Zhou, T. Yildirim, *J. Phys. Chem. Lett.* **2010**, *1*, 1946–1951.

[13] a) J. V. Smith, L. S. D. Glasser, F. Rinaldi, *Acta Crystallogr.* **1963**, *16*, 45–53; b) J. V. Smith, *Acta Crystallogr.* **1962**, *15*, 835–845.

[14] a) F. Gao, J. H. Kwak, J. Szanyi, C. H. F. Peden, *Top. Catal.* **2013**, *56*, 1441–1459; b) D. W. Fickel, J. M. Fedeyko, R. F. Lobo, *J. Phys. Chem. C* **2010**, *114*, 1633–1640.

[15] D. H. Olson, M. A. Camblor, L. A. Villaescusa, G. H. Kuehl, *Microporous Mesoporous Mater.* **2004**, *67*, 27–33.

[16] a) M. Miyamoto, Y. Fujiokax, K. Yogo, *J. Mater. Chem.* **2012**, *22*, 20186–20189; b) J. Shang, G. Li, R. Singh, Q. F. Gu, K. M. Nairn, T. J. Bastow, N. Medhekar, C. M. Doherty, A. J. Hill, J. Z. Liu, P. A. Webley, *J. Am. Chem. Soc.* **2012**, *134*, 19246–19253; c) J. Shang, G. Li, R. Singh, P. Xiao, J. Z. Liu, P. A. Webley, *J. Phys. Chem. C* **2010**, *114*, 22025–22031.

[17] a) L. J. Smith, H. Eckert, A. K. Cheetham, *Chem. Mater.* **2001**, *13*, 385–391; b) L. J. Smith, H. Eckert, A. K. Cheetham, *J. Am. Chem. Soc.* **2000**, *122*, 1700–1708.

[18] B. Civalleri, A. M. Ferrari, M. Llunell, R. Orlando, M. Merawa, P. Ugliengo, *Chem. Mater.* **2003**, *15*, 3996–4004.

[19] a) T. Frising, P. Leflaive, *Microporous Mesoporous Mater.* **2008**, *114*, 27–63; b) G. Vitale, C. F. Mellot, L. M. Bull, A. K. Cheetham, *J. Phys. Chem. B* **1997**, *101*, 4559–4564; c) M. Feuerstein, R. F. Lobo, *Chem. Mater.* **1998**, *10*, 2197–2204.

[20] a) M. P. Attfield, A. W. Sleight, *Chem. Commun.* **1998**, 601–602; b) D. A. Woodcock, P. Lightfoot, P. A. Wright, L. A. Villaescusa, M. J. Diaz-Caba-nas, M. A. Camblor, *J. Mater. Chem.* **1999**, *9*, 349–351; c) D. A. Woodcock, P. Lightfoot, L. A. Villaescusa, M. J. Diaz-Cabanas, M. A. Camblor, D. Engberg, *Chem. Mater.* **1999**, *11*, 2508–2514.

[21] a) A. K. A. Pryde, K. D. Hammonds, M. T. Dove, V. Heine, J. D. Gale, M. C. Warren, *J. Phys. Condens. Matter* **1996**, *8*, 10973–10982; b) K. D. Hammonds, V. Heine, M. T. Dove, *J. Phys. Chem. B* **1998**, *102*, 1759–1767.

[22] C. Graham, D. A. Imrie, R. E. Raab, *Mol. Phys.* **1998**, *93*, 49–56.

[23] A. Simon, K. Peters, *Acta Crystallogr. Sect. B* **1980**, *36*, 2750–2751.

[24] a) D. Bonenfant, M. Kharoune, P. Niquette, M. Mimeault, R. Hausler, *Sci. Technol. Adv. Mater.* **2008**, *9*, 013007; b) M. Palomino, A. Corma, F. Rey, S. Valencia, *Langmuir* **2010**, *26*, 1910–1917.

[25] A. Zukal, A. Pulido, B. Gil, P. Nachtigall, O. Bludsky, M. Rubes, J. Cejka, *Phys. Chem. Chem. Phys.* **2010**, *12*, 6413–6422.

[26] F. Akhtar, Q. L. Liu, N. Hedin, L. Bergstrom, *Energy Environ. Sci.* **2012**, *5*, 9947–9947.

[27] a) R. C. Deka, R. K. Roy, K. Hirao, *Chem. Phys. Lett.* **2000**, *332*, 576–582; b) T. L. Ho, *Chem. Rev.* **1975**, *75*, 1–20.

[28] P. Mignon, P. Geerlings, R. Schoonheydt, *J. Phys. Chem. B* **2006**, *110*, 24947–24954.

[29] M. J. Díaz-Cabañas, P. A. Barrett, M. A. Camblor, *Chem. Commun.* **1998**, 1881–1882.

[30] J. Shang, G. Li, Q. Gu, R. Singh, P. Xiao, J. Z. Liu, P. A. Webley, *Chem. Commun.* **2014**, *50*, 4544–4546.

[31] a) B. H. Toby, *J. Appl. Crystallogr.* **2001**, *34*, 210–213; b) A. C. L. a. R. B. V. Dreele, *Los Alamos National Laboratory Report, LAUR* **1994**, *86*.

These are not the final page numbers! ↗↗

FULL PAPERS

Window of opportunity: Li, Na, K, and Si chabazite zeolites were investigated by in situ powder diffraction. Two adsorption sites for CO_2 were found in all samples with CO_2 adsorption in the 8-membered ring window being dominant with end-on coordination to alkali-metal cations also observed. Li and Na chabazite with Si/Al = 6 have adsorption capacity comparable to low-silica commercial faujasite and linde type A zeolite at ambient temperature and pressure.
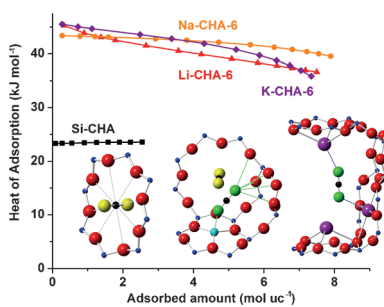
T. D. Pham, M. R. Hudson, C. M. Brown,* R. F. Lobo*

■■ – ■■

Molecular Basis for the High CO_2 Adsorption Capacity of Chabazite Zeolites

These are not the final page numbers! ↗↗